American Journal of Physics

COMPUTATIONAL PHYSICS | AUGUST 01 2026

Tracking the spread of chaos in the swinging Atwood machine

Nick Tufillaro

Am. J. Phys. 94, 688–695 (2026)
https://doi.org/10.1119/5.0344894

The Computational Physics Section publishes articles that help students and instructors learn about the computational tools used in contemporary research. Interested authors are encouraged to send a proposal to the editors of the Section, Jan Tobochnik (jant@kzoo.edu) or Harvey Gould (hgould@clarku.edu). Summarize the physics and the algorithm you wish to discuss and how the material would be accessible to advanced undergraduates or beginning graduate students.

Tracking the spread of chaos in the swinging Atwood machine

Nick Tufillaro[a)]
Aqualytics, P. O. Box 1028, Corvallis, Oregon 97333

(Received 8 May 2026; accepted 23 May 2026)

Chaos is investigated in the swinging Atwood machine as the mass ratio μ decreases from the integrable motion at $\mu = 3$ to mostly chaotic dynamics at $\mu = 2.7$. The spread of chaos is characterized by combining a stability index with a Poincaré surface of section. An effective computational solution requires a consideration of numerical overflow issues. Once these are resolved, the computation shows that the spread of chaos, in this parameter regime, is associated with a hyperbolic periodic loop orbit. The example illustrates how to incorporate computational physics—such as the regularization of a singularity—into the undergraduate curriculum.
https://doi.org/10.1119/5.0344894

I. INTRODUCTION

The swinging Atwood machine is a tractable problem both theoretically[1] and experimentally[2,3] for undergraduates studying classical mechanics. Recall that one of the masses (m) in the Atwood machine is allowed to swing in the plane (Fig. 1). If we assume that the masses are connected by frictionless, massless pulleys, the Hamiltonian for the swinging Atwood machine is

$$H = \frac{1}{2}\left(\frac{p_r^2}{\mu+1} + \frac{p_\theta^2}{r^2}\right) + gr(\mu - \cos\theta), \tag{1}$$

where p_r and p_θ are the conjugate momenta, g is gravitational acceleration, and $\mu = M/m$ is the mass ratio. We focus on how the dynamics depend on the parameter μ. Without loss of generality, we set $m = 1$ in the Hamiltonian, which effectively rescales the energy. (Because the potential function is homogeneous, orbits at different energies are similar.[4])

The swinging Atwood machine is integrable for the mass ratio $\mu = 3$ and chaotic for all other mass ratios.[5,6] An *integrable system* is a perfectly predictable Hamiltonian system. Formally, a system with N degrees of freedom is Liouville integrable if it possesses exactly N independent, conserved quantities (constants of motion) I_i that are in involution,

$$\{I_i, I_j\} = 0 \quad \text{and} \quad \{I_i, H\} = 0 \quad \text{for} \quad i,j = 1,\ldots,N, \tag{2}$$

where $\{\cdot,\cdot\}$ denotes the Poisson bracket. Physically, these strict constraints preclude chaotic behavior. The constants of motion confine the phase-space trajectories entirely to smooth, invariant N-dimensional geometric surfaces known as *KAM tori*.[7]

For a mechanical system with two degrees of freedom, we can think of the torus as the surface of a donut in phase space. Every orbit of the machine forms a path on this donut. The *rotation number* characterizes the average rate at which a trajectory winds around the two fundamental angular cycles of the donut. The rotation number is defined as the ratio of the system's two characteristic frequencies, $\rho = \omega_1/\omega_2$. If this ratio is rational ($\rho = p/q$, where p and q are integers), the orbit eventually closes on itself, forming a periodic trajectory. Conversely, if the rotation number is irrational, the orbit is quasiperiodic, never repeats, and densely fills the surface of the torus.[8]

As the system moves away from integrable motion, tori dissolve based on stability conditions that are a function of the rotation number,[9–11] and stable regions of phase space (periodic or quasiperiodic orbits) are replaced by unstable regions (chaotic orbits).

In this paper, we examine how chaos spreads as the mass ratio decreases from integrable (stable) motion, specifically as μ decreases from 3 to 2.7. Numerical experiments reveal that the geometric feature governing the spread of chaos in this parameter regime is an unstable periodic orbit associated with a collision between the swinging mass and the pulley. In the language of dynamical systems, chaos spreads as part of the bifurcation process leading to the merger of an unstable homoclinic orbit and its elliptical partner—a saddle-center bifurcation of periodic orbits—and the regions of stable and chaotic orbits are roughly delineated by the stable and unstable manifolds of this homoclinic orbit.[12] This mechanism of chaos is easy to visualize: orbits that start very close are suddenly far apart after they fly off to the left or to the right during a near collision with the pulley. This behavior is analogous to the origin of chaos in a forced pendulum,

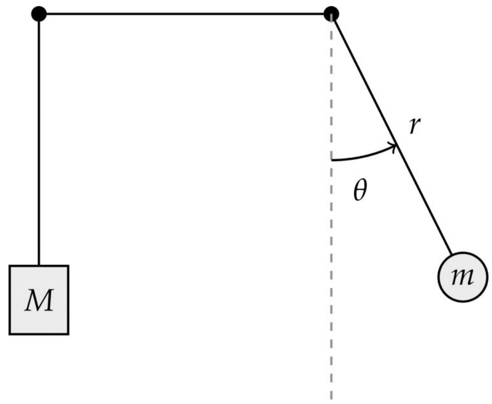

Fig. 1. The swinging Atwood's machine.

where orbits approaching the unstable equilibrium (the inverted pendulum) fall chaotically to the left or right depending on the system's state.[13,14]

To investigate chaos in the swinging Atwood machine, we proceed in the usual way.[15,16] First, we visualize the global dynamics as a function of μ using a Poincaré surface of section.[17] A surface of section is a geometric technique that simplifies a complex, continuous trajectory by taking a lower-dimensional "slice" of the phase space. By recording a data point only when the orbit intersects this designated plane in a specific direction, the continuous flow of the system is reduced to a discrete map. This dimension reduction makes it much easier to visually distinguish between constrained orderly motion and chaotic wandering. We identify geometrical structures in phase space—namely, the low-order periodic orbits and their stable and unstable manifolds that shepherd the flow as μ is varied from 3 (integrable) to 2.7 (mostly chaotic)—and track the overall spread of chaos using the smaller alignment index discussed in Sec. III. The theoretical and computational aspects are well covered in books and papers,[18–21] as well as by commonly available numerical toolkits,[22–25] and thus we do not delve much into the methods here, except for two aspects of the computational solution.

In Sec. II, we discuss regularization, or how to deal with the "division by zero" in the dynamical equations. In Sec. III, we discuss variational integration, or how to handle overflow in the Jacobian matrix through continuous normalization. After resolving these computational issues, we present in Sec. IV the results on tracking the initial breakdown of integrable motion. Although details vary from problem to problem, properly identifying and solving issues of overflow or underflow are ubiquitous in computational physics, and investigating the spread of chaos in the swinging Atwood machine provides an introduction to some of the numerical challenges.

Problem 1. Derive the equations of motion $(\dot{r}, \dot{\theta}, \dot{p}_r, \dot{p}_\theta)$ for the swinging Atwood machine from the Hamiltonian in Eq. (1). Use the energy constant E to develop a formula for $p_r = K(E, g, \mu, r, \theta, p_\theta)$. Use your function to write a program to numerically integrate and plot (r, θ) for a few orbits assuming $g = 9.81$, $E = 2g$, $\theta_0 = 0$, and period T. Some initial conditions to explore are (μ, r_0, p_{r0}, T): (a) (3, 0.50, 6.26, 2.49), (b) (2.95, 0.51, 6.08, 2.54), (c) (2.99, 0.10, 0.73, 2.56), (d) (2.95, 0.19, 1.52, 2.58), (e) (2.95, 0.51, 5.84, 100), and (f) (2.95, 0.125, 2.61, 100). To help the reader get started, the supplementary material includes instructions for how to install and run a Runge–Kutta–Fehlberg solver using the GNU Plotutils package on most operating systems.[23]

II. FIXING THE COLLISION SINGULARITY

To construct a surface of section, we need to numerically create the trajectories for a long time. However, a severe numerical issue arises because as the swinging mass approaches the pulley ($r \to 0$), the angular velocity $\dot{\theta} = p_\theta / r^2$ rapidly approaches infinity. This $1/r^2$ singularity crashes standard numerical ordinary differential equation algorithms due to infinite derivatives and truncation errors.

To overcome this problem, we use the technique known as *regularization*, which was originally developed for astronomical simulations[26] and consists of introducing a fictitious time variable τ, related to physical time t by the transformation

$$dt = r^2\, d\tau. \tag{3}$$

We use this transformation to construct an extended phase space Γ that includes the physical time t as a state variable,

$$\begin{aligned}\Gamma &= r^2(H - E)\\ &= \frac{r^2 p_r^2}{2(1+\mu)} + \frac{1}{2}p_\theta^2 + g r^3(\mu - \cos\theta) - E r^2 = 0.\end{aligned} \tag{4}$$

For high-velocity motion near the pulley, the angular momentum is approximately conserved—the gravitational term in the equations of motion is negligible compared to the terms associated with the angular momentum. This new (approximate and localized) invariant indirectly motivates us to look for a transformation that examines the dynamics at the origin in more detail, which we do by slowing down the "clock" as the mass approaches the singularity at $r = 0$.

Specifically, we multiply the Hamiltonian by a scaling function $g(r, \theta) = r^2$ and define a new dynamical system on an extended phase space as $\Gamma = r^2(H - E) = 0$. Multiplication by r^2 clears the problematic $1/r^2$ singularity present in the angular term (see your equations of motion derived in Problem 1). Furthermore, because the equations in this extended space dictate that $dt/d\tau = \partial\Gamma/\partial(-E)$, this choice seamlessly enforces our desired time transformation, $dt = r^2\, d\tau$. With the new time τ, we obtain the regularized equations of motion (denoted by primes $d/d\tau$),

$$r' = \frac{\partial \Gamma}{\partial p_r} = \frac{r^2 p_r}{1+\mu}, \tag{5}$$

$$\theta' = \frac{\partial \Gamma}{\partial p_\theta} = p_\theta, \tag{6}$$

$$p_r' = -\frac{\partial \Gamma}{\partial r} = -\frac{r p_r^2}{1+\mu} - 3 g r^2(\mu - \cos\theta) + 2Er, \tag{7}$$

$$p_\theta' = -\frac{\partial \Gamma}{\partial \theta} = -g r^3 \sin\theta, \tag{8}$$

$$t' = \frac{\partial \Gamma}{\partial(-E)} = r^2. \tag{9}$$

Even if the mass passes exactly through the pulley ($r = 0$), the right-hand sides remain well-behaved and do not blow up to infinity.

The new variable effectively slows down time near the collision, making fixed-step size simulations very inefficient. Therefore, an adaptive step size method is required to solve the equations using regularization. We used the Dormand–Prince (RK45) method.[27,28] This adaptive solver computes two simultaneous solutions at each time step: one fourth-order and one fifth-order. The magnitude of the difference between these two state vectors provides an estimate of the local truncation error. To control the step size, this estimated error is compared against a maximum allowable error threshold, which is calculated dynamically for each state variable using the prescribed relative and absolute tolerances (10^{-8} and 10^{-10}, respectively), scaling the relative tolerance by the current magnitude of the state. If the estimated error exceeds this threshold, the step is rejected and the step size shrinks; if it is within the threshold, the step is accepted and the step size can safely grow for the next iteration.

Problem 2. Use Hamilton's equations to transform the equations of motion via the regularization transform, Eq. (3), and arrive at Eqs. (5)–(9). Is the system described by Γ in Eq. (4) Hamiltonian? Is the regularization transform a canonical transformation?[1]

A Poincaré surface of section reduces the complexity of the four-dimensional (4D) phase space $(r, \theta, p_r, p_\theta)$ to a 2D plot. Because the energy E is conserved, the accessible states are restricted to a 3D energy shell.[29] We take a 2D slice through this shell by recording the system state only when it crosses a specific geometric plane. In our analysis, this plane is defined at $\theta = 0$ (the pendulum hanging straight down) with the mass moving in the positive angular direction ($p_\theta > 0$). The resulting intersections are plotted in the remaining coordinates (r, p_r), which define a (nonglobal) Poincaré surface of section.[17]

Solving a grid of initial conditions (r_0, p_{r0}) while varying μ (with fixed E) allows us to explore how the global dynamics depends on μ. Regions with continuous curves on the surface of section indicate stable, quasiperiodic invariant tori, while scattered "dust" indicates unstable regions with chaotic orbits.

III. DISTINGUISHING STABLE FROM UNSTABLE ORBITS

To evaluate the stability of an orbit, we look at the evolution of small perturbations using the variational equations constructed with the Jacobian matrix. Consider an n-dimensional continuous dynamical system defined by

$$\frac{d\mathbf{x}}{dt} = \mathbf{f}(\mathbf{x}(t)), \tag{10}$$

where $\mathbf{x} \in \mathbb{R}^n$ represents the state vector. Let $\mathbf{x}(t)$ be the reference trajectory, and $\mathbf{x}(t) + \mathbf{w}(t)$ a perturbed trajectory. Linearizing the dynamics via a Taylor expansion yields the variational equations

$$\frac{d\mathbf{w}}{dt} = J(\mathbf{x}(t))\,\mathbf{w}(t), \tag{11}$$

where $J(\mathbf{x}) = \partial\mathbf{f}/\partial\mathbf{x}$ is the $n \times n$ Jacobian matrix evaluated along the reference trajectory.

For the swinging Atwood machine in standard physical time t, the state vector is $\mathbf{x}_{\text{orig}} = (r, \theta, p_r, p_\theta)^T$ and the corresponding 4×4 Jacobian matrix J_{orig} is

$$J_{\text{orig}}(\mathbf{x}_{\text{orig}}) = \begin{bmatrix} 0 & 0 & \frac{1}{\mu+1} & 0 \\ -\frac{2p_\theta}{r^3} & 0 & 0 & \frac{1}{r^2} \\ -\frac{3p_\theta^2}{r^4} & -g\sin\theta & 0 & \frac{2p_\theta}{r^3} \\ -g\sin\theta & -gr\cos\theta & 0 & 0 \end{bmatrix}. \tag{12}$$

When tracking trajectories using the regularization technique described in Sec. II, the system is integrated with respect to the fictitious time τ. This extended phase space introduces physical time as a fifth state variable, making the state vector $\mathbf{x}_{\text{reg}} = (r, \theta, p_r, p_\theta, t)^T$. We differentiate the regularized equations of motion, which yields the 5×5 Jacobian matrix J_{reg} to obtain

$$J_{\text{reg}}(\mathbf{x}_{\text{reg}}) = \begin{bmatrix} \frac{2rp_r}{\mu+1} & 0 & \frac{r^2}{\mu+1} & 0 & 0 \\ 0 & 0 & 0 & 1 & 0 \\ -\frac{p_r^2}{\mu+1} - 6gr(\mu - \cos\theta) + 2E & -3gr^2\sin\theta & -\frac{2rp_r}{\mu+1} & 0 & 0 \\ -3gr^2\sin\theta & -gr^3\cos\theta & 0 & 0 & 0 \\ 2r & 0 & 0 & 0 & 0 \end{bmatrix}. \tag{13}$$

In a chaotic regime, the distance between infinitesimally close trajectories diverges exponentially. The magnitude of the deviation vector grows as $\|\mathbf{w}(t)\| \sim e^{\lambda_1 t}$, where $\lambda_1 > 0$ is the maximum Lyapunov exponent. When integrating the equations of motion numerically using standard double-precision floating-point arithmetic (which caps at approximately 10^{308}), chaotic orbits will cause $\|\mathbf{w}(t)\|$ to overflow, resulting in a `NaN` (Not a Number) system failure within seconds.

However, as described in the following, to distinguish chaotic orbits from stable orbits, we need only to track the direction of the deviation vectors, not their magnitude. We can therefore restrict the solver to integrating unit vectors $\hat{\mathbf{w}} = \mathbf{w}/\|\mathbf{w}\|$. Although discrete normalization at each integration step is an option, a numerically stable approach is continuous normalization built directly into the numerical algorithm. We take the time derivative of $\hat{\mathbf{w}}$,

$$\frac{d}{dt}\hat{\mathbf{w}} = \frac{d}{dt}\left(\frac{\mathbf{w}}{(\mathbf{w}^T\mathbf{w})^{1/2}}\right), \tag{14}$$

apply the quotient rule, and substitute $\dot{\mathbf{w}} = J\mathbf{w}$ to find

$$\frac{d\hat{\mathbf{w}}}{dt} = \frac{\dot{\mathbf{w}}}{\|\mathbf{w}\|} - \frac{\mathbf{w}}{\|\mathbf{w}\|^3}(\mathbf{w}^T\dot{\mathbf{w}}) = J\hat{\mathbf{w}} - \hat{\mathbf{w}}(\hat{\mathbf{w}}^T J\hat{\mathbf{w}}). \tag{15}$$

This equation acts as an intrinsic Gram–Schmidt orthogonal projection. The term $(\hat{\mathbf{w}}^T J\hat{\mathbf{w}})\hat{\mathbf{w}}$ subtracts any growth in the direction of $\hat{\mathbf{w}}$, guaranteeing that $d/dt\|\hat{\mathbf{w}}\|^2 = 0$. By appending Eq. (14) to the physical state equations, floating-point overflow is eliminated.

The smaller alignment index (SALI) method takes advantage of the stretching nature of chaotic phase space to quickly distinguish between stable and unstable orbits.[30] Suppose we initialize two independent, orthonormal deviation vectors, $\hat{\mathbf{w}}_1(0)$ and $\hat{\mathbf{w}}_2(0)$. In a stable/quasiperiodic orbit, the motion is confined to an invariant torus. Without an exponentially dominant stretching direction, the two deviation vectors fluctuate and drift, but they remain linearly independent and do not permanently align. In an unstable/chaotic orbit, the phase space possesses at least one direction of exponential stretching. As the system evolves, the flow aggressively pulls both $\hat{\mathbf{w}}_1$ and $\hat{\mathbf{w}}_2$ to point along the direction of maximal expansion. Because the vectors are normalized, they will either become identical (parallel) or exact opposites (anti-parallel) (see Fig. 2).

To quantify this geometrical alignment, the smaller alignment index is defined as the minimum between the sum and the difference of the two normalized deviation vectors,

$$\mathrm{SALI}(t) = \min(\|\hat{\mathbf{w}}_1(t) + \hat{\mathbf{w}}_2(t)\|,\ \|\hat{\mathbf{w}}_1(t) - \hat{\mathbf{w}}_2(t)\|). \tag{16}$$

If the vectors align parallel ($\hat{\mathbf{w}}_1 \to \hat{\mathbf{w}}_2$), their difference approaches zero. If they align anti-parallel ($\hat{\mathbf{w}}_1 \to -\hat{\mathbf{w}}_2$), their sum approaches zero. In either case, the smaller alignment index plummets.

Problem 3. The initial conditions (a)-(d) in Problem 1 are periodic orbits. Use these orbits as seed values to use in a 'root finding' algorithm with 'analytic continuation' to track

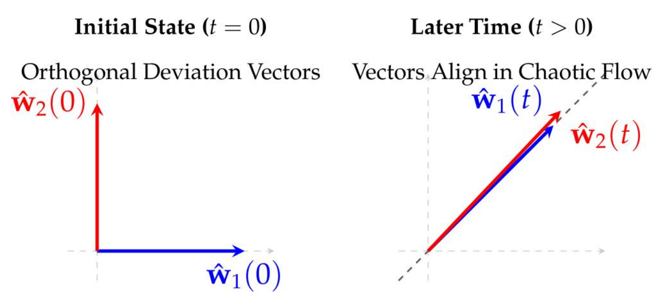

Fig. 2. (Color online) The smaller alignment index (SALI) tracks the alignment of perturbation vectors. Initially orthogonal vectors (left) are stretched by a chaotic flow (right), eventually aligning parallel to the axis of maximal expansion.

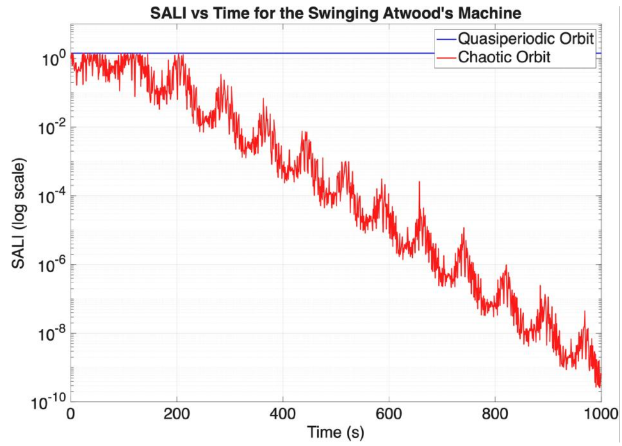

Fig. 3. (Color online) An example of how the time-dependence of the smaller alignment index can distinguish between quasiperiodic (stable) and chaotic (unstable) orbits in the swinging Atwood machine. Initial conditions from Problem 1(e), quasiperiodic, and Problem 1(f), chaotic, are used.

the location of these orbits as μ varies from 3 down to 2.77, in steps of 0.01. Provide a list containing μ, the initial conditions, the period, the eigenvalues, and a classification of the orbit type (elliptic, hyperbolic). Use a toolbox or develop your own code with the method outlined in Appendix A.

Problem 4. Use the quasiperiodic initial condition from Problem 1(e) and the chaotic initial condition from Problem 1(f) to create a figure similar to Fig. 3, illustrating how the smaller alignment index varies in time and can be used to distinguish quasiperiodic orbits from chaotic orbits (see Appendix B).

IV. TRACKING THE SPREAD OF CHAOS

To track the spread of chaos, we estimate the percentage of unstable orbits relative to the total number of orbits by numerically sampling phase space using the surface of section. This procedure is illustrated in Fig. 4, which shows how phase space contains a greater percentage of chaotic orbits as the system moves from integrable motion at $\mu = 3$ toward $\mu = 2.9$, 2.8, and 2.7.

The stability of each orbit in the surfaces of section is evaluated and colored according to its estimated stability index. In the color map, a blue hue indicates stability and a red hue instability. A single threshold is applied to the stability index ($\log_{10}(\mathrm{SALI}) < -8$) to quantitatively evaluate the spread of chaos. The percentage is a simple estimate; a range of percentages is possible depending on the exact parameters chosen. However, the overall trends (increasing or decreasing) are similar for reasonable choices of the parameters.

Figure 5 shows a plot of the spread of chaos as μ decreases from 3 to 2.7. As indicated by visual inspection, the percentage of phase space occupied by chaotic orbits decreases (more or less) monotonically from $\mu = 3$ to 2.7. With a basic grounding in dynamical systems, it is easy to identify the geometrical mechanism causing the spread of chaos—namely, a low-order hyperbolic periodic orbit that moves toward its partner elliptic periodic orbit and in the process appears to destroy KAM tori as it approaches a saddle-center bifurcation, which numerics indicate occurs at $\mu \approx 2.77$. The spread of chaos in this example, from integrable motion to chaotic motion arising from an unstable orbit that separates different regimes of motion, has been termed *separatrix*

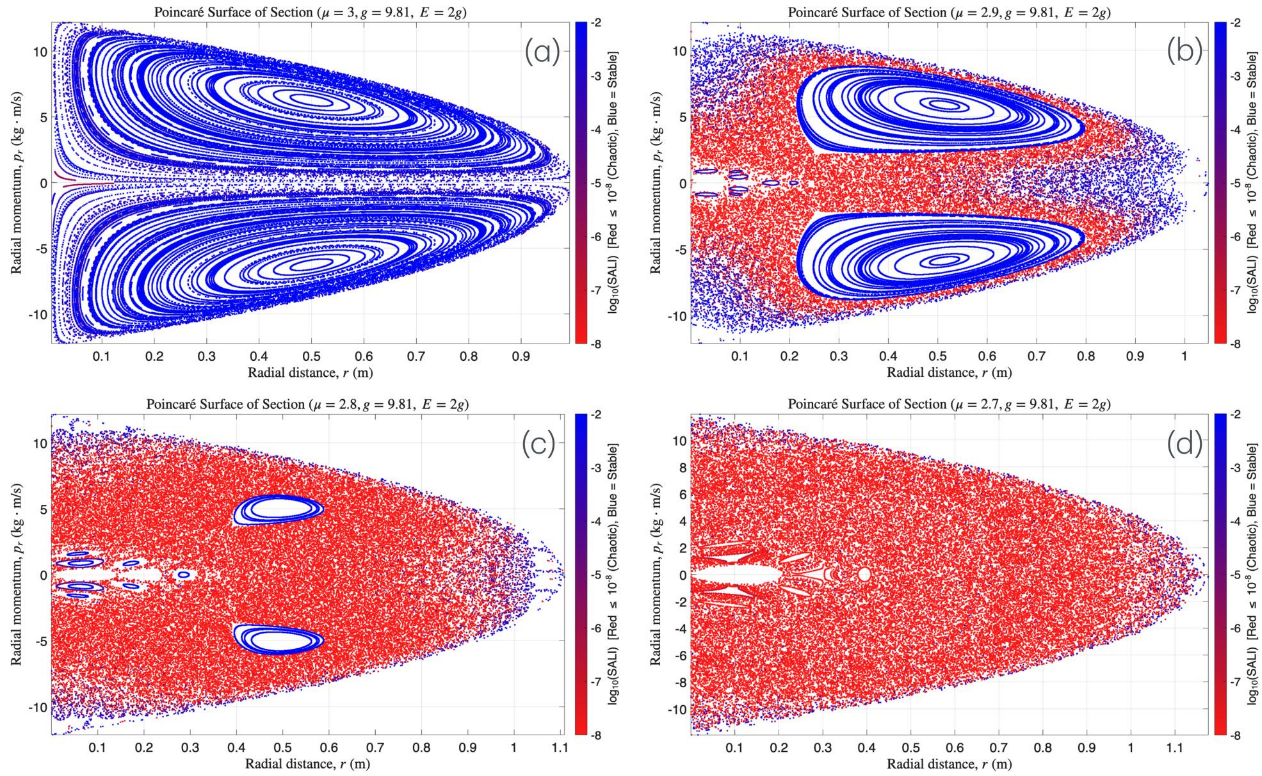

Fig. 4. (Color online) A sequence of surfaces of section for decreasing mass ratios: (a) $\mu = 3$, integrable, stratified by tori; (b) $\mu = 2.9$, nonintegrable, KAM tori and chaos; (c) $\mu = 2.8$, increasingly chaotic as the tori are destroyed; and (d) $\mu = 2.7$, mostly chaotic.

chaos, and can be studied in more detail using Hamiltonian perturbation theory.[31,32]

In the study of dynamical systems, a *separatrix* is a boundary in phase space that divides distinct types of motion.[15,20] Consider a pendulum.[19,33] It has two primary modes of behavior: *libration*—small oscillations around the stable equilibrium (the bottom)—and *rotation*—full circular revolutions (when given enough energy). The curve that separates these two behaviors is the separatrix. Physically, it represents the trajectory where the pendulum has exactly enough energy to reach the upright vertical position and stay there (an unstable equilibrium). In an ideal, integrable system (like the frictionless pendulum), the separatrix is a smooth, well-defined boundary. When a small perturbation is applied, the separatrix also points to a generic mechanism to generate chaos. The approach to the unstable position along the separatrix—an unstable equilibrium point in the pendulum, or an unstable periodic orbit in the swinging Atwood machine—can result in the system becoming extremely sensitive to even the smallest external influence near this boundary. The geometrical remnants of the separatrix in the perturbed system are the stable (W^s) and unstable manifolds (W^u). Regions near a hyperbolic point of phase space generate chaotic behavior because the flow is ripped apart near these geometric structures, and the way the flow comes back together can be very complicated, as discovered by Poincaré.[34] According to the *Smale–Birkhoff homoclinic theorem*,[35] if stable and unstable manifolds in the perturbed system intersect once transversally, they must intersect an infinite number of times, creating a homoclinic tangle. This single point of an isolated (i.e., transversal) intersection forces an infinite number of other intersections, resulting in a region of "stochasticity" where the trajectory is chaotic and exhibits sensitive dependence on initial conditions.

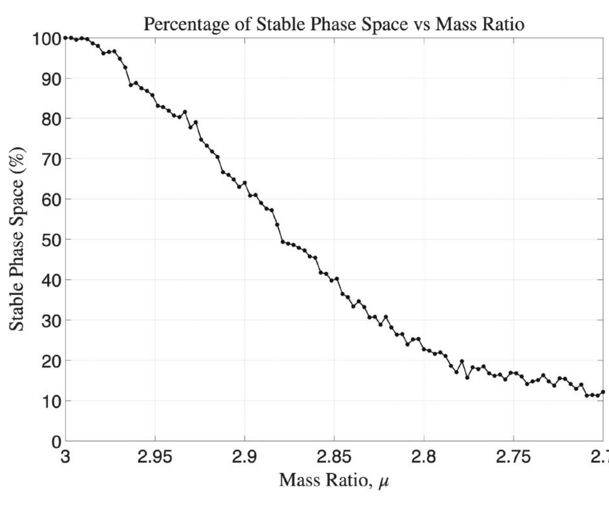

Fig. 5. Estimated percentage of phase space with stable orbits as a function of the mass ratio μ.

The hyperbolic point organizing the chaotic regions of the swinging Atwood machine near $\mu = 3$ is easy to spot in the surface of section. As shown in Fig. 6 for $\mu = 2.95$, both the elliptic fixed point and the hyperbolic fixed point correspond to two separate, coexisting periodic loop orbits in configuration space. We call the stable orbit [blue curve in Fig. 6(b)] the *stable loop*, and the hyperbolic orbit [red curve in Fig. 6(b)] the *unstable loop*. By analytic continuation, we can follow these orbits back to their integrable ($\mu = 3$) locations. The stable loop at $\mu = 3$ is the central fixed point in Fig. 4(a) surrounded by elliptic tori, while the

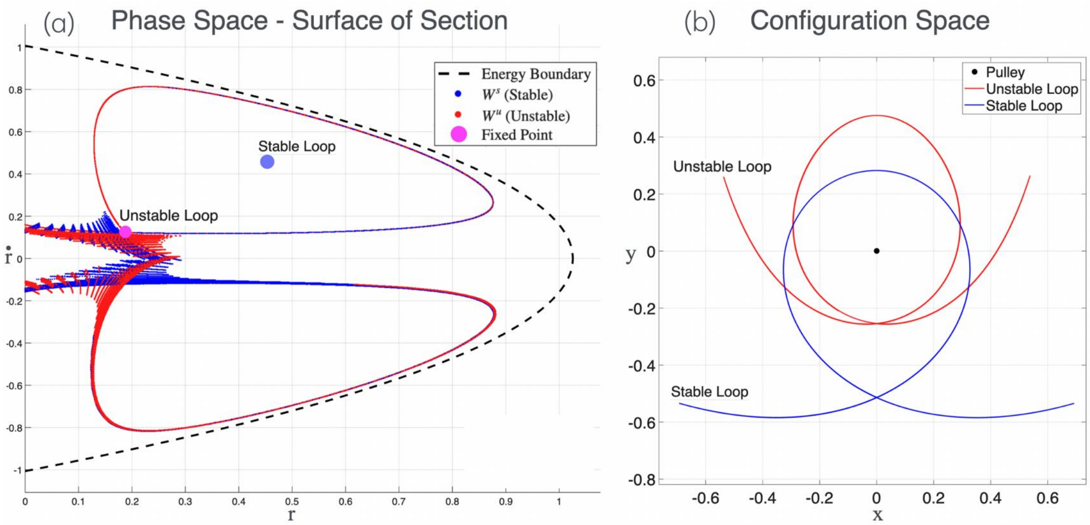

Fig. 6. (Color online) (a) The fixed points in the phase-space surface of section and (b) their corresponding loop periodic orbits in configuration space. The stable loop orbit corresponds to an elliptic fixed point in phase space that organizes the main collection of KAM tori when $2.7 < \mu < 3$. Branches of the stable (W^s) and unstable (W^u) manifolds of the hyperbolic homoclinic point [purple point in (a)] demarcate the main stable and unstable regions in phase space.

unstable loop corresponds to an orbit that starts to fall directly above the pulley ($\theta_0 = \pi$), wraps tightly around the pulley once, and then shoots upward. When it reaches the top, it falls once again and repeats. As described in Ref. 8, when $\mu = 3.0$, all the orbits of the swinging Atwood machine in phase space are pinched between two periodic orbits. In the middle, there is a (singular tori) stable loop periodic orbit which has more or less the same shape as that shown in Fig. 6(b) (blue curve). On the outside in phase space, surrounding all the tori, is an unstable orbit like that shown in Fig. 6(b) (red curve). As μ approaches 3, in configuration space the unstable loop becomes more tightly bound around the pulley and the ends of the orbit face straight up.

The unstable loop, which in the limit $\mu = 3$ collides with the pulley, is the origin of most of the unstable motion in the swinging Atwood machine for $\mu \in [2.77, 3)$.

Problem 5. Using a dynamical systems toolkit (such as those available for Python[25] or Julia,[24] or the codes in the supplementary material), create a surface of section plot like those in Fig. 4 for $\mu = 2.95$. Identify the unstable loop and the stable loop in the plot.

SUPPLEMENTARY MATERIAL

Please click on this link to access the supplementary material, package contains computer codes and simulations that provide problem solutions, and can be a useful starting point for students looking to further explore the swinging Atwood machine's dynamics or similar Hamiltonian systems. For instance, does the golden ratio appear in the last torus?[36] Print readers can see the supplementary material at https://doi.org/10.60893/figshare.ajp.c.8494659.

AUTHOR DECLARATIONS

Conflict of Interest

The author has no conflicts to disclose.

APPENDIX A: TRACKING PERIODIC ORBITS

To study periodic orbits, we reduce the continuous-time dynamics to a discrete map by introducing a Poincaré section Σ. We define Σ as the plane where the swinging mass crosses the vertical axis with positive angular momentum,

$$\Sigma = \{(r, \theta, p_r, p_\theta) \in \mathbb{R}^4 \,|\, \theta = 0, p_\theta > 0, H = E\}. \qquad \text{(A1)}$$

On this section, the state is completely parameterized by the vector $\mathbf{X} = [r, p_r]^T$. The angular momentum p_θ is uniquely determined by solving $H = E$ for p_θ,

$$p_\theta = \sqrt{2r^2\left(E - \frac{p_r^2}{2(\mu+1)} - gr(\mu - 1)\right)}. \qquad \text{(A2)}$$

A periodic orbit of a continuous system corresponds to a fixed point of the Poincaré return map $P : \Sigma \to \Sigma$. The map $P(\mathbf{X})$ integrates Hamilton's equations from an initial state $\mathbf{X}$ on Σ until the trajectory next intersects Σ.

Finding a periodic orbit reduces to solving the nonlinear root-finding problem,

$$\mathbf{F}(\mathbf{X}) = P(\mathbf{X}) - \mathbf{X} = \mathbf{0}. \qquad \text{(A3)}$$

The program `po_stable` in the supplementary material uses a shooting method paired with a standard Newton–Raphson or trust-region solver.[28] Given an initial guess $\mathbf{X}^{(0)}$, the solver iteratively refines the guess until the discrepancy $\|P(\mathbf{X}) - \mathbf{X}\|$ is below a strict tolerance (e.g., 10^{-10}).

To track how the periodic orbit evolves as μ is continuously varied from $\mu = 3.0$ to $\mu = 2.77$, we employ zeroth-order numerical continuation. Let $\mathbf{X}^*(\mu)$ denote the exact fixed point of the return map for a specific value of μ. If we change μ by a small $\Delta\mu$, the new fixed point $\mathbf{X}^*(\mu + \Delta\mu)$ will be located close to $\mathbf{X}^*(\mu)$ assuming the orbit does not undergo a catastrophic bifurcation. The continuation algorithm proceeds as follows:

(1) Start at $\mu_0 = 3.0$ with a known fixed point $\mathbf{X}^*(\mu_0)$.

(2) Decrease the parameter: $\mu_{i+1} = \mu_i - \Delta\mu$.
(3) Use the solution from the previous step as the initial guess for the current step: $\mathbf{X}_{\text{guess}} = \mathbf{X}^*(\mu_i)$.
(4) Solve $\mathbf{F}(\mathbf{X};\, \mu_{i+1}) = \mathbf{0}$ using the shooting method to find $\mathbf{X}^*(\mu_{i+1})$.
(5) Repeat until the target μ is reached.

This method relies on the implicit function theorem, ensuring that a unique continuous branch of periodic orbits exists as long as the Jacobian of $\mathbf{F}$ is nonsingular.

Once a periodic orbit $\mathbf{X}^*$ is found, its linear stability is determined by evaluating how small perturbations $\delta\mathbf{X}$ behave over one full period. This stability is evaluated with the Jacobian of the Poincaré map evaluated at the fixed point, also known as the monodromy matrix $\mathbf{M}$,

$$\mathbf{M} = \frac{\partial P(\mathbf{X})}{\partial \mathbf{X}}\bigg|_{\mathbf{X}^*} = \begin{bmatrix} \dfrac{\partial r'}{\partial r} & \dfrac{\partial r'}{\partial p_r} \\ \dfrac{\partial p_r'}{\partial r} & \dfrac{\partial p_r'}{\partial p_r} \end{bmatrix}. \tag{A4}$$

Because we lack a closed-form expression for $P(\mathbf{X})$, we estimate $\mathbf{M}$ using central finite differences. For a small perturbation $\epsilon \approx 10^{-6}$,

$$\mathbf{M}_{:,1} \approx \frac{P\left(\mathbf{X}^* + [\epsilon, 0]^T\right) - P\left(\mathbf{X}^* - [\epsilon, 0]^T\right)}{2\epsilon}, \tag{A5}$$

$$\mathbf{M}_{:,2} \approx \frac{P\left(\mathbf{X}^* + [0, \epsilon]^T\right) - P\left(\mathbf{X}^* - [0, \epsilon]^T\right)}{2\epsilon}. \tag{A6}$$

Liouville's theorem dictates that Hamiltonian phase volume is conserved, making the Poincaré map area-preserving. Consequently, the determinant of the monodromy matrix must be identically one ($\det(\mathbf{M}) = 1$).

The eigenvalues λ_1, λ_2 of $\mathbf{M}$ are found via the characteristic polynomial

$$\lambda^2 - \mathrm{Tr}(\mathbf{M})\,\lambda + \det(\mathbf{M}) = 0 \Rightarrow \lambda^2 - \mathrm{Tr}(\mathbf{M})\,\lambda + 1 = 0. \tag{A7}$$

The solutions are completely determined by the trace of the monodromy matrix, $\mathrm{Tr}(\mathbf{M}) = m_{11} + m_{22}$,

$$\lambda_{1,2} = \frac{\mathrm{Tr}(\mathbf{M}) \pm \sqrt{\mathrm{Tr}(\mathbf{M})^2 - 4}}{2}. \tag{A8}$$

The trace of the monodromy matrix provides a straightforward classification of the orbit's stability:

- **Elliptic (stable):** If $|\mathrm{Tr}(\mathbf{M})| < 2$, the discriminant is negative. The eigenvalues are complex conjugates residing exactly on the unit circle in the complex plane ($|\lambda_{1,2}| = 1$, $\lambda = e^{\pm i\phi}$). Small perturbations oscillate quasiperiodically around the fixed point.
- **Hyperbolic (unstable):** If $|\mathrm{Tr}(\mathbf{M})| > 2$, the discriminant is positive. The eigenvalues are strictly real, with one greater than 1 ($\lambda_1 > 1$) and the other less than 1 ($\lambda_2 = 1/\lambda_1 < 1$). The orbit possesses distinct stable and unstable manifolds, leading to exponential divergence of trajectories.
- **Parabolic (marginal):** If $|\mathrm{Tr}(\mathbf{M})| = 2$, the eigenvalues are degenerate ($\lambda_1 = \lambda_2 = \pm 1$). This typically signals a bifurcation point where the orbit changes stability type or spawns new periodic orbits as μ is varied.

APPENDIX B: THE SMALLER ALIGNMENT INDEX (SALI) METHOD

To compute the smaller alignment index, we must track the evolution of infinitesimal perturbations to the trajectory. Let $\mathbf{w}(t) = [\delta r, \delta\theta, \delta p_r, \delta p_\theta]^T$ be a deviation vector in the tangent space of the trajectory $\mathbf{X}(t)$.

The evolution of $\mathbf{w}(t)$ is governed by the variational equations, obtained by linearizing the vector field $\mathbf{f}(\mathbf{X})$ around the reference trajectory,

$$\dot{\mathbf{w}} = \mathbf{A}(\mathbf{X})\,\mathbf{w}, \tag{B1}$$

where $\mathbf{A}(\mathbf{X})$ is the Jacobian matrix evaluated continuously along the orbit.

The SALI computation requires the simultaneous integration of the main orbit and two independent deviation vectors.

Step 1: Initialization. Choose an initial state $\mathbf{X}(0)$ on the desired energy surface. Choose two orthogonal, normalized initial deviation vectors, for example,

$$\mathbf{w}_1(0) = [1, 0, 0, 0]^T, \quad \mathbf{w}_2(0) = [0, 1, 0, 0]^T. \tag{B2}$$

Construct the extended 12-dimensional state vector $\mathbf{Y} = [\mathbf{X}, \mathbf{w}_1, \mathbf{w}_2]^T$.

Step 2: Integration and normalization. Integrate the extended system $(\dot{\mathbf{X}}, \dot{\mathbf{w}}_1, \dot{\mathbf{w}}_2)$ forward in time using a high-precision numerical algorithm. Because chaotic dynamics will cause the magnitudes of $\mathbf{w}_1$ and $\mathbf{w}_2$ to grow exponentially, they will quickly overflow machine precision. To prevent this, the integration is performed in small time steps Δt. At the end of each step, the vectors are normalized,

$$\hat{\mathbf{w}}_1 = \frac{\mathbf{w}_1}{\|\mathbf{w}_1\|}, \quad \hat{\mathbf{w}}_2 = \frac{\mathbf{w}_2}{\|\mathbf{w}_2\|}. \tag{B3}$$

The normalized vectors are then used as the initial conditions for the next integration step.

Step 3: Calculating the index. At each time step t, the smaller alignment index is defined as the minimum of the norms of the sum and difference of the two normalized deviation vectors:

$$\mathrm{SALI}(t) = \min(\|\hat{\mathbf{w}}_1(t) + \hat{\mathbf{w}}_2(t)\|,\ \|\hat{\mathbf{w}}_1(t) - \hat{\mathbf{w}}_2(t)\|). \tag{B4}$$

The behavior of $\mathrm{SALI}(t)$ sharply distinguishes the underlying dynamics:

- **Chaotic orbits:** In a chaotic region, any arbitrary initial deviation vector will stretch and rapidly align along the most unstable manifold (the direction of the maximum Lyapunov exponent). As both $\mathbf{w}_1$ and $\mathbf{w}_2$ align with this same dominant direction, they become either parallel ($\hat{\mathbf{w}}_1 \approx \hat{\mathbf{w}}_2$) or anti-parallel ($\hat{\mathbf{w}}_1 \approx -\hat{\mathbf{w}}_2$). Consequently, either their difference or their sum approaches zero. Thus, for chaotic orbits, $\mathrm{SALI}(t)$ drops exponentially to the limit of machine precision ($\sim 10^{-16}$).
- **Regular (quasiperiodic) orbits:** In a regular region, there is no exponential divergence. The deviation vectors oscillate and generally remain linearly independent,

exploring the tangent space of the invariant torus. Therefore, $\mathrm{SALI}(t)$ fluctuates around a positive nonzero constant (typically $\mathcal{O}(1)$).

By plotting $\log(\mathrm{SALI})$ vs time, we can visually identify the nature of the orbit, often much faster than waiting for the convergence of a Lyapunov exponent calculation.

[a)]Electronic mail: nick@aqualytics.eco, ORCID: 0009-0006-2896-8832.

[1]Nivaldo A. Lemos, *Analytical Mechanics* (Cambridge U. P., 2018).
[2]O. Pujol, J. P. Pérez, J. P. Ramis, C. Simó, S. Simon, and J. A. Weil, "Swinging Atwood machine: Experimental and numerical results, and a theoretical study," Physica D **239**(12), 1067–1081 (2010).
[3]Nicholas Tufillaro, "Smiles and teardrops," Undergraduate thesis (Reed College, 1982).
[4]Regilene Oliveira and Claudia Valls, "Polynomial integrability of Hamiltonian systems with homogeneous potentials of degree $-k$.," Phys. Lett. A **380**(46), 3876–3880 (2016).
[5]J. Casasayas, A. Nunes, and N. Tufillaro, "Swinging Atwood's machine: Integrability and dynamics," J. Phys. **51**(16), 1693–1702 (1990).
[6]Regina Martínez and Carles Simó, "Non-integrability of the degenerate cases of the Swinging Atwood's Machine using higher order variational equations," Discrete Contin. Dyn. Syst. **31**(1), 1–24 (2011).
[7]Rafael De la Llave *et al*., "A tutorial on KAM theory," in *Proceedings of Symposia in Pure Mathematics* (American Mathematical Society, Providence, RI, 2001), Vol. 69, pp. 175–296.
[8]Ana Nunes, Josefina Casasayas, and Nicholas Tufillaro, "Periodic orbits of the integrable swinging Atwood's machine," Am. J. Phys. **63**(2), 121–126 (1995).
[9]M. A. M. de Aguiar, C. P. Malta, M. Baranger, and K. T. R. Davies, "Bifurcations of periodic trajectories in non-integrable Hamiltonian systems with two degrees of freedom: Numerical and analytical results," Ann. Phys. **180**(2), 167–205 (1987).
[10]M. A. M. De Aguiar and Michel Baranger, "Invariant tori for two-dimensional non-integrable Hamiltonians," Ann. Phys. **186**(2), 355–380 (1988).
[11]K. Efstathiou and N. Voglis, "A method for accurate computation of the rotation and the twist numbers of invariant circles," Physica D **158**(1–4), 151–163 (2001).
[12]Robert L. Devaney, "Homoclinic orbits in Hamiltonian systems," J. Differ. Equations **21**(2), 431–438 (1976).
[13]Philip Holmes, Jerrold Marsden, and Jürgen Scheurle, "Exponentially small splittings of separatrices with applications to KAM theory and degenerate bifurcations," Contemp. Math. **81**, 213–244 (1988).
[14]Amadeu Delshams and Teresa M. Seara, "An asymptotic expression for the splitting of separatrices of the rapidly forced pendulum," Commun. Math. Phys. **150**(3), 433–463 (1992).
[15]Todd Timberlake, "A computational approach to teaching conservative chaos," Am. J. Phys. **72**(8), 1002–1007 (2004).
[16]Carles Simó, "Measuring the total amount of chaos in some Hamiltonian systems," Discrete Contin. Dyn. Syst. **34**(12), 5135–5164 (2014).
[17]H. R. Dullin and A. Wittek, "Complete Poincaré sections and tangent sets," J. Phys. A **28**(24), 7157–7180 (1995).
[18]Nicholas B. Tufillaro, Tyler Abbott, and Jeremiah Reilly, *An Experimental Approach to Nonlinear Dynamics and Chaos* (Addison-Wesley, Redwood City, CA, 1992). https://aquahue.net/aquahue/books/an_experimental_approach.pdf.
[19]P. Coullet, J. M. Gilli, M. Monticelli, and N. Vandenberghe, "A damped pendulum forced with a constant torque," Am. J. Phys. **73**(12), 1122–1128 (2005).
[20]H. J. Korsch, E. M. Graefe, and Hans-Jörg Jodl, "The kicked rotor: Computer-based studies of chaotic dynamics," Am. J. Phys. **76**(4), 498–503 (2008).
[21]Steven H. Strogatz, *Nonlinear Dynamics and Chaos: With Applications to Physics, Biology, Chemistry, and Engineering* (Chapman and Hall/CRC, 2024).
[22]N. Tufillaro and G. A. Ross, "ODE: A program for the numerical solution of ordinary differential equations," Technical Report No. 83-52321-39 (Bell Laboratories, Murray Hill, NJ, 1983).
[23]Robert S. Maier and Nicholas B. Tufillaro, see https://www.gnu.org/software/plotutils/manual/en/plotutils.pdf for "The GNU Plotting Utilities" (2009).
[24]George Datseris, "DynamicalSystems.jl: A Julia software library for chaos and nonlinear dynamics," J. Open. Source Software **3**(23), 598 (2018).
[25]Matheus Rolim Sales, Leonardo Costa de Souza, Daniel Borin, Michele Mugnaine, José Danilo Szezech, Ricardo Luiz Viana, Iberê Luiz Caldas, Edson Denis Leonel, and Chris G. Antonopoulos, "pynamicalsys: A Python toolkit for the analysis of dynamical systems," Chaos, Solitons Fractals **201**, 117269 (2025).
[26]Javier Roa, *Regularization in Orbital Mechanics: Theory and Practice* (Walter de Gruyter GmbH & Co KG, 2017), Vol. 42.
[27]Ernst Hairer, Syvert P. Nørsett, and Gerhard Wanner, *Solving Ordinary Differential Equations I: Nonstiff Problems* (Springer, 1993).
[28]Andrew R. Conn, Nicholas I. M. Gould, and Philippe L. Toint, *Trust Region Methods* (SIAM, 2000).
[29]A. Ouazzani-TH and M. Ouazzani-Jamil, "Bifurcations of Liouville tori of an integrable case of swinging Atwood's machine," Il Nuovo Cimento B **110**(9), 1111–1121 (1995).
[30]Ch Skokos, Ch Antonopoulos, T. C. Bountis, and M. N. Vrahatis, "Detecting order and chaos in Hamiltonian systems by the SALI method," J. Phys. A **37**(24), 6269–6284 (2004).
[31]G. M. Zaslavskiĭ and N. N. Filonenko, "Stochastic instability of trapped particles and conditions of applicability of the quasi-linear approximation," Sov. J. Exp. Theor. Phys. **27**(5), 851–857 (1968).
[32]Regina Martínez and Carles Simó, "Return maps, dynamical consequences and applications," Qual. Theory Dyn. Syst. **14**(2), 353–379 (2015).
[33]Robert DeSerio, "Chaotic pendulum: The complete attractor," Am. J. Phys. **71**(3), 250–257 (2003).
[34]Henri Poincaré, *The Three-Body Problem and the Equations of Dynamics: Poincaré's Foundational Work on Dynamical Systems Theory* (Springer, 2017).
[35]Clark Robinson, *Dynamical Systems: Stability, Symbolic Dynamics, and Chaos* (CRC Press, 1998).
[36]Erik M. Bollt and James D. Meiss, "Controlling chaotic transport through recurrence," Physica D **81**(3), 280–294 (1995). This paper is dedicated to the memory of Dr. Erik Bollt (1967–2025).